

# We are IntechOpen, the world's leading publisher of Open Access books Built by scientists, for scientists

6,900

Open access books available

186,000

International authors and editors

200M

Downloads

Our authors are among the

154

Countries delivered to

TOP 1%

most cited scientists

12.2%

Contributors from top 500 universities



WEB OF SCIENCE™

Selection of our books indexed in the Book Citation Index  
in Web of Science™ Core Collection (BKCI)

Interested in publishing with us?  
Contact [book.department@intechopen.com](mailto:book.department@intechopen.com)

Numbers displayed above are based on latest data collected.  
For more information visit [www.intechopen.com](http://www.intechopen.com)



# Inversely Designed Scramjet Flow-Path

*Mookesh Dhanasar, Frederick Ferguson and Julio Mendez*

## Abstract

It can be argued that at the heart of functional hypersonic vehicle is its engine. Key to a functionally efficient scramjet engine lies in the design of its flow-path. The flow-path is made up of the following sections: (1) the forebody inlet; (2) the isolator, (3) the combustor, and (4) the nozzle. This chapter focuses on the design of the forebody inlet and the isolator sections of a scramjet engine. In this framework, key to a functionally efficient scramjet engine lies in the design of its flow-path. This flow-path design must consider a complex flow-field physics and the interaction of physical surfaces with this complex flow-field. Many attempts to design efficient scramjet flow-paths have met with some measured degree of success. This research uses a 'inverse design' approach, which is similar to Darwin's theory of evolution, where an organism adapts to survive in its environment; the scramjet flow-path will be carved/extracted from the operational environment. The objective is to naturally and organically capture, process and direct the flow from the environment; thus preparing it for the combustion process. This approach uses the ideal 2-D oblique shock relations, coupled with Nonweiler's caret waverider theory and streamline marching techniques.

**Keywords:** scramjet flow-path, hypersonic propulsion, inverse design, stream tube, oblique shockwave, Billig's isolator relations, Nonweiler's caret waverider

## 1. Introduction

Driven by the desire to improve air travel and shorten flight time, aircraft engines have evolved from simple reciprocating internal combustion engines to advance axial flow jet engines. Jet engines fall into several categories. These include air-breathing, turbine powered, turbojet, turbofan, ramjet compression and scramjet compression engines. Ramjet and scramjet compression engines are unique in that they represent the latest development on the evolutionary path of jet engines. The ramjet, unlike conventional jet engines which uses turbine driven compressors to compress the incoming air, uses shockwaves to achieve this goal. The compressed air is burnt in the combustor under sub-sonic conditions. The scramjet is basically an air-breathing jet engine designed to fly at hypersonic speeds between Mach 4 and 12 or speeds in the range of 1207–2995 m/s (2700–6700 mph). A scramjet engine captures its airflow from the atmosphere and also compresses it across shockwaves before the air enters the combustor. Fuel is injected into the combustor where combustion occurs under supersonic conditions. The hot, high-pressure gas leaving the combustor is then accelerated to high velocities in the nozzle to produce thrust as it exits the engine.

Generally speaking, the concepts associated with scramjet engines appear at first glance to be very simple. This however is very misleading as attempts develop a working scramjet engine that has proven to be quite an engineering challenge. Several aspects of scramjet engine development are at various stages of development. These include supersonic fuel-air mixing, aero-thermodynamic heat dissipation from both skin friction and internal combustion, and other thermal management problems associated with operating an engine at exceedingly high temperatures for extended periods of time. Combustion chamber components could experience temperatures on the order of over 3033 K (5000°F). At these temperatures most metals melt and fluids (air and fuel) ionize, making the physics of their associated behavior unpredictable.

This chapter focuses on the design concepts for the forebody, inlet, and isolator sections of an innovative scramjet engine geometry and some of its flow physics.

## 2. Inverse scramjet 2-D centerline design approach

As stated earlier, the scramjet concept represents the latest evolution in the series of air-breathing jet engines. Combustion in these engines occurs under supersonic conditions. Scramjet engines are seen as the propulsion system that is at the heart of hypersonic vehicles/platforms. Every scramjet conceptual engine design and engines flown to-date all have a common set of components or sub-sections. **Figure 1** presents these components/sub-sections for a pod-mounted conceptual scramjet design. These components/sections are the forebody section, the inlet section, isolator section, combustor section, and the diffuser-nozzle section. Ideally, the engine concept presented should be able to function over a wide range of Mach numbers. This gives rise to the idea of a morphing ramjet/scramjet or dual mode scramjet configurations as presented in **Figure 2** [1]. **Figure 2a**, presents the dual mode scramjet engine, **Figure 2b**, the pure scramjet mode and **Figure 2c**, the pure ramjet mode.

A typical dual mode scramjet configuration as that presented in **Figure 3**, was inversely carved out of supersonic and hypersonic flow-fields. The design framework used in the design of the forebody, inlet and isolator sections forms the core of this chapter.

## 3. Scramjet inverse design approach

The inverse design approach relies on extracting the configuration of interest from the environment in which it operates. For this design process the centerline

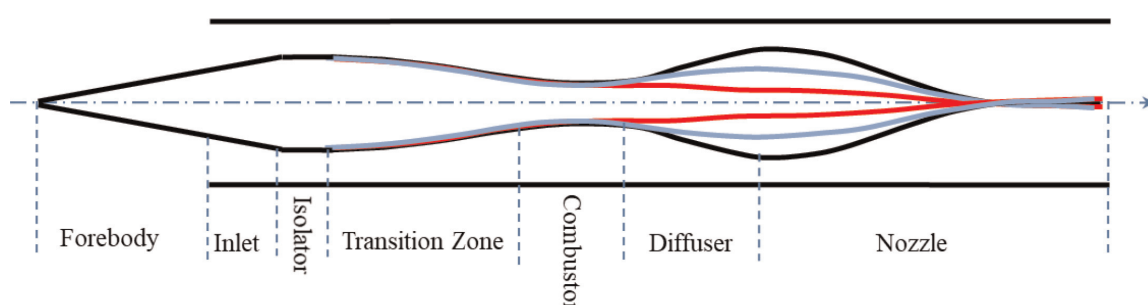


**Figure 1.**  
*Pod-mounted scramjet concept.*

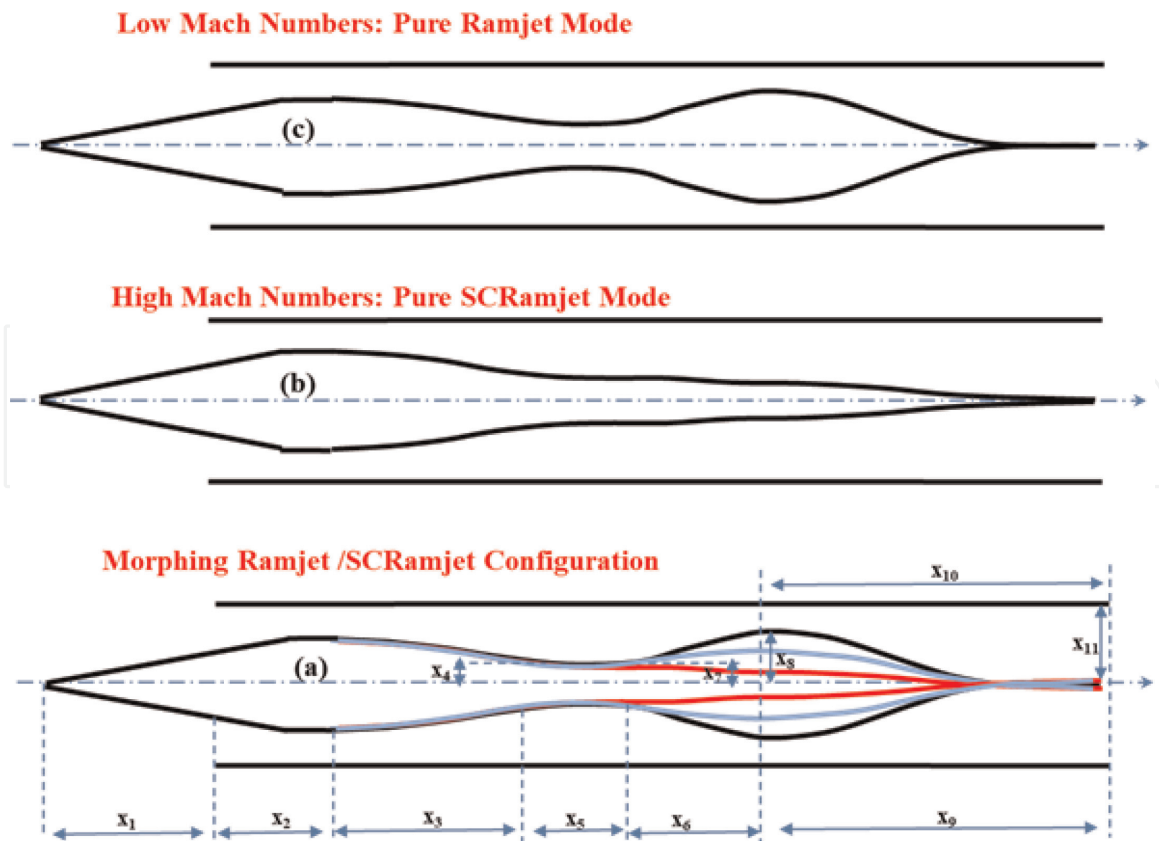


Figure 2.  
 Dual-mode scramjet concept.

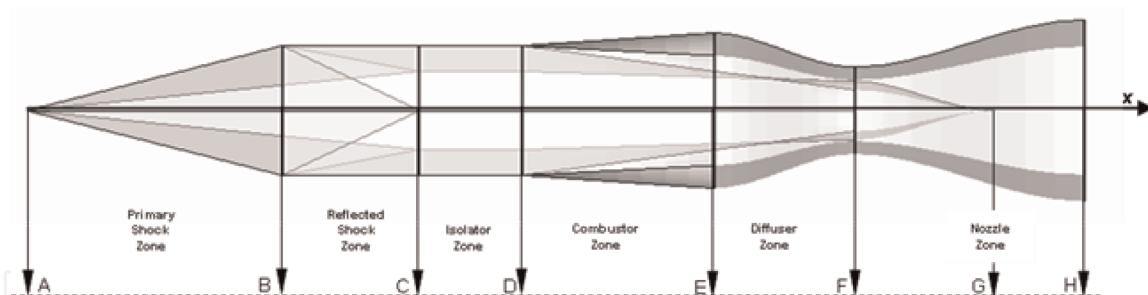
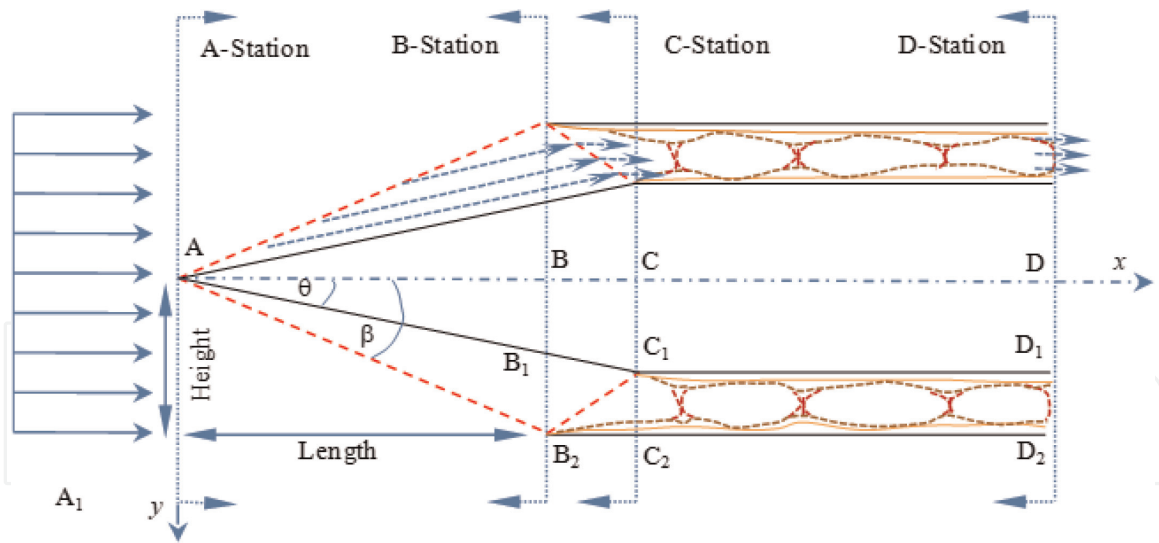


Figure 3.  
 Illustration of the cross section of the scramjet.

geometry of a given 2-D scramjet configuration is explicitly constructed using the following design inputs: freestream Mach number,  $M_\infty$ , scramjet forebody length,  $L$ , shock angle,  $\beta$ , caret angle,  $\alpha$ , cruising flight altitude,  $H_\infty$ , and isolator back-pressure ratio,  $P_{in}/P_{exit}$ . All freestream flow-field properties are extracted from the Mach number and altitude [3–6]. This information is used in the construction, analysis and definition of the three fundamental aerodynamic zones, namely; the ‘primary shock’ zone AB, the ‘reflected shock zone’, BC, and the ‘isolator zone’, CD as presented in Figure 4. Also presented in Figure 4 is a 2-dimensional conceptual representation of the flow-field physics associated with supersonic flow interaction over a wedge and in a constant area duct. Details of this flow-field physics and its exploitation in the inverse design approach are explained in the next section. Also addressed is the derivation of the actual 3-dimensional forebody section. This is a



**Figure 4.** Conceptual 2-D centerline cross-section of the forebody-inlet-isolator scramjet section with flow physics representation.

two-step process, where in step one, the 2-D construction of the ‘forebody’, domain A-D, is conducted. Step two is where the 3-D geometry is obtained.

### 3.1 Aerodynamics of the 2-D ‘forebody’ configuration

Consider the 2-D cross-sectional illustration of the scramjet forebody-inlet-isolator section presented in **Figure 4**. Now consider a supersonic flow travelling parallel to the x-axis of a 2-D wedge. Supersonic aerodynamics dictates that the flow is deflected first by the oblique shock wave,  $AB_2$ , originating from the leading edge, A, of the wedge. The flow is deflected a second time by a reflected shock wave,  $B_2C_1$  emanating from the cowl lip at point  $B_2$ , of the inlet. The flow enters the isolator duct and travels once more in a direction that is parallel to the x-axis. To ensure that the flow in the isolator duct remain supersonic the freestream Mach number must be greater than 3.0 and the shock wave angle,  $\beta$ , greater than 12 and less than 30 degrees.

The flow-field behavior within the isolator duct is of paramount importance. This flow-field may consist of a system of oblique or normal shocks, as visualized in **Figure 4**. Driving this behavior is the flow-field vicious interactions with the isolator duct walls. The isolator’s non-dimensional length,  $L/H$ , and the pressure differential at the duct’s entrance and exit also enhance the flow-field’s behavior.

### 3.2 Derivation of the 2-D ‘forebody-inlet-isolator’ configuration

The ‘forebody-inlet-isolator’ concept presented in **Figure 4** relies on determining the geometric design points located at stations A, B, C and D, along the x-axis of the scramjet. This is accomplished by use of the oblique shock relations described in [2–7] and the ‘isolator’ relations that were experimentally derived in [8–9]. It is assumed that in **Figure 4** the flow travels in the x-direction, and that the construction of the ‘forebody’ configuration starts at design point, A. The following account details the logic used to define the locations of design points A, B, C and D:

#### 3.2.1 Design point at station A

The design point at station A is considered the origin of the scramjet design coordinate system, therefore, design point A coordinates are evaluated as follows,  $A_x = 0$ ,  $A_y = 0$ , and  $A_z = 0$ .

### 3.2.2 Design points at station B

Using the input data, the location of design point B, can be computed with the use of the following relations:  $B_x = L$ ,  $B_y = 0$ , and  $B_z = 0$ .

In addition, using trigonometric relationships design point  $B_1$  is evaluated as follows:  $B_{1x} = B_x$ ,  $B_{1y} = B_x \tan(\theta)$  and  $B_{1z} = 0$ .

The coordinates for design point  $B_2$  are evaluated in the following manner:  $B_{2x} = B_x$ ,  $B_{2y} = B_x \tan(\beta)$ , and  $B_{2z} = 0$ . The wedge angle is represented by theta ( $\theta$ ) and the shock angle is represented by beta ( $\beta$ ). Using the Mach number and the shock angle beta ( $\beta$ ), the wedge angle theta ( $\theta$ ) can be obtained with the use of the Theta-Beta-Mach ( $\theta$ - $\beta$ -M) relationship [2–7] given as seen in Eq. (1). In Eq. (1) the constant  $\gamma$  is set at a value of 1.4.

$$\theta = \text{atan} \left\{ 2 \cot \beta \left[ \frac{M_\infty^2 \sin^2 \beta - 1}{M_\infty^2 (\gamma + \cos 2\beta) + 2} \right] \right\} \quad (1)$$

### 3.2.3 Design points at station C

The design points at station C is extracted from the wedge angle,  $\theta$ , and the flow-field properties behind the primary shock wave,  $AB_2$ , as seen in **Figure 4**. Determination of the location of design point C is a little more involved and is approached systematically as outlined in the following steps:

- a. First, the Mach number, M, behind the primary shock wave,  $AB_2$  (see **Figure 4**), is obtained using Eq. (2),

$$M = \left\{ \frac{1}{\sin(\beta - \theta)} \right\} \frac{[1 + [(\gamma - 1)/2](M_\infty \sin(\beta))^2]}{[\gamma(M_\infty \sin(\beta))^2 - (\gamma - 1)/2]} \quad (2)$$

- b. This Mach number, coupled with the free stream parameters are then used with the oblique shock relations derived in [5] for the evaluation of all of flow-field properties behind the primary shock,  $AB_2$ . The flow-field properties, pressure, P, temperature, T, density,  $\rho$ , and total pressure,  $P_{t,2}$ , are evaluated using Eqs. (3)–(6).

$$\frac{P}{P_\infty} = \frac{2\gamma(M_\infty \sin \beta)^2 - (\gamma - 1)}{(\gamma + 1)} \quad (3)$$

$$\frac{T}{T_\infty} = \frac{[2\gamma(M_\infty \sin \beta)^2 - (\gamma - 1)] [(\gamma + 1)(M_\infty \sin \beta)^2 + 2]}{(\gamma + 1)^2 (M_\infty \sin \beta)^2} \quad (4)$$

$$\frac{\rho}{\rho_\infty} = \frac{(\gamma + 1)(M_\infty \sin \beta)^2}{(\gamma - 1)(M_\infty \sin \beta)^2 + 2} \quad (5)$$

$$\frac{P_{t,2}}{P_{t,\infty}} = \left[ \frac{(\gamma + 1)(M_\infty \sin \beta)^2}{(\gamma - 1)(M_\infty \sin \beta)^2 + 2} \right]^{\frac{\gamma}{\gamma-1}} \left[ \frac{(\gamma + 1)}{2\gamma(M_\infty \sin \beta)^2 - (\gamma - 1)} \right]^{\frac{1}{\gamma-1}} \quad (6)$$

- c.  $B_2C_1$  as seen in **Figure 4** represent the reflected shock wave. This reflected shock wave is a the result of a flow-field behind the primary shock wave,  $AB_2$ , with a supersonic Mach number, M, once more being deflected by an imaginary wedge, with wedge angle  $\theta$  at design point  $B_2$ . This imaginary wedge

is oriented in such a manner that it ensures that the deflected flow travels parallel to the x-axis, **Figure 4**. At this stage updated values for the wedge angle,  $\theta$  and the Mach number,  $M$ , are obtained using Eqs. (1) and (2). A reflection shock angle,  $\phi$  is now be defined as  $\phi = \beta_1 - \theta$ . In this expression,  $\beta_1$  is the reflected shock angle. This reflected shock angle is generated by the interaction of the flow-field with Mach number  $M$  and the imaginary wedge with angle  $\theta$ . Note that  $\beta_1$  is obtained using Eq. (1) and replacing the value of the freestream Mach number,  $M_\infty$ , with that of the supersonic Mach number,  $M$ .

- d. The flow-field properties behind the reflected shock wave  $B_2C_1$  are now obtained in a similar manner as described in 'b' above. Eq. (2) is used to obtain  $M_1$ , which is the Mach number behind the reflected shock. In Eq. (2) the freestream Mach number,  $M_\infty$ , is replaced with Mach number  $M$ . It is very important to note here that  $M_1$  represents the Mach number at the entrance to the isolator section of the scramjet. Eqs. (3)–(6) are used to derive the additional flow-field properties of pressure, temperature, density and total temperature,  $p_1$ ,  $T_1$ ,  $\rho_1$  and  $T_o$ , behind the reflected shock. Note that in these equations the value for the freestream Mach number,  $M_\infty$ , is now replaced with the value of the Mach number,  $M$ , from the flow-field properties behind the primary shock.
- e. Having obtained the parameters,  $\theta$ ,  $\beta$  and  $\beta_1$  all design points at station C can now be derived. The y-coordinate and z-coordinate are defined as  $C_y = 0$ , and  $C_z = 0$ , respectively. The x-coordinate is obtained with the help of trigonometric relations, and is defined as:

$$C_x = \left[ 1 + \frac{\tan(\beta) - \tan(\theta)}{\tan(\theta) - \tan(\beta_1 - \theta)} \right] B_x \quad (7)$$

- f. The coordinates of point  $C_1$  are determined as follows:  $C_{1x} = C_x$ ,  $C_{1y} = C_x \tan(\theta)$ , and  $C_{1z} = 0$ .
- g. Similarly, the coordinates of point  $C_2$  are determined from:  $C_{2x} = C_x$ ,  $C_{2y} = B_{2y}$ , and  $C_{2z} = 0$ .

#### 3.2.4 Design points at station D

The evaluation of the coordinates of the design points at station D is also a multi-step process.

- a. First a non-dimensional expression for the 'normal total' pressure value,  $P_{n,in}$ , is derived, Eq. (8). This expression is a function of isolator entrance conditions, where  $M_1$  is treated as the  $M_{in}$ , and the static pressure,  $P_1$ , as  $P_{in}$ . Note here that the values of  $M_1$  and  $P_1$  are obtained from the flow-field properties behind the reflected shock  $B_2C_1$ .

$$\frac{P_{n,in}}{P_{in}} = \left[ \frac{2\gamma M_1^2 - (\gamma - 1)}{(\gamma + 1)} \right] \quad (8)$$

In determining the isolator length for a design process, the ratio of the entrance to exit pressures,  $P_{in}/P_{out}$ , over the range between  $P_{in}$  and  $P_{n,in}$  has to be evaluated. This value is needed to determine the length of an isolator that can reliably prevent

all ‘unstart’ conditions. In this design process, the ratio,  $P_{out}/P_{n,in}$ , representing the isolator exit pressure,  $P_{out}$ , to the ‘normal total’ pressure value,  $P_{n,in}$ , is prescribed. Using this approach, the value for  $P_{in}/P_{out}$  can be determined by using Eq. (9):

$$\frac{P_{out}}{P_{in}} = \left( \frac{P_{out}}{P_{n,in}} \right) \left( \frac{P_{n,in}}{P_{in}} \right) \quad (9)$$

b. The system of 1-D conservation laws result in the following expression for the isolator exit Mach number,  $M_{out}$  [8, 9];

$$M_{out} = \left\{ \frac{\gamma^2 M_{in}^2 [1 + ((\gamma - 1)/2) M_{in}^2]}{(1 - \gamma M_{in}^2 - P_{out}/P_{in})^2} - \left( \frac{\gamma - 1}{2} \right) \right\}^{-\frac{1}{2}} \quad (10)$$

Similarly, with the exit Mach number known, the non-dimensional length of the isolator can be evaluated based on the following experimental relationship developed in [8, 9]:

$$\left( \frac{L}{H} \right)_{Isolator} = \frac{\sqrt{\theta/H} \left\{ 50((P_{out}/P_{in}) + 1) + 170((P_{out}/P_{in}) - 1)^2 \right\}}{(Re_{\theta})^{\frac{1}{4}} M_{in}^2 - 1} \quad (11)$$

where  $Re_{\theta}$  is the inlet Reynolds number based on the momentum thickness. Also, the symbol,  $H$ , represents the isolator height that is determined from the y-coordinates of points  $C_2$  and  $C_1$ , in a manner such that,  $H = C_{2y} - C_{1y}$ .

- c. The coordinates of point D are computed as follows:  $D_x = C_x + L_{Isolator}$ ,  $D_y = 0$ , and  $D_z = 0$ .
- d. The coordinates of point  $D_1$  are computed as follows:  $D_{1x} = D_x$ ,  $D_{1y} = C_{1y}$ , and  $D_{1z} = 0$ .
- e. The coordinates of point  $D_2$  are computed as follows:  $D_{2x} = D_x$ ,  $D_{2y} = C_{2y}$ , and  $D_{2z} = 0$ .

Finally, with the coordinates of all the design points at all stations, A, B,  $B_1$ ,  $B_2$ , C,  $C_1$ ,  $C_2$ , D,  $D_1$ , and  $D_2$ , fully defined, the sketch illustrated in **Figure 4** can be constructed.

## 4. 3-D computer aided design (CAD) design

### 4.1 Overview of the 3-D design process

The 3-D design process has as its origin in the inversely design two-dimensional geometry extracted from a 2-D hypersonic flow-field. This is then coupled with the Nonweiler’s waverider approach [10] of inversely carving stream surfaces from inviscid flow-fields. A caret waverider, **Figure 5**, is chosen as an example because it represents a 3-D geometry that was obtained from a 2-D flow-field. This caret waverider geometry is constructed from a single planer shock wave,  $AB_3B_4$ , as seen in **Figure 5**. A unique feature of this construction process is that at any cross-section of the waverider geometry there is a wedge that is supported by an oblique shock wave, with these wedges being parallel to the flow.

In reality, the caret waverider is carved from an inverse design approach that relies on the inviscid streamline principle. This principle states that any inviscid streamline can be replaced by a solid wall. The principle also states that replacing the inviscid streamline with a solid wall has no effect on the external flow. Planar inviscid stream surfaces are formed from these inviscid streamlines. These inviscid stream surfaces are then brought together to construct 3-D inviscid waverider geometries and stream tubes. An examination of **Figure 5** demonstrates how the streamlines form planar stream surfaces, such as, upper inviscid surfaces,  $ABB_3$  and  $ABB_4$ , or lower stream surfaces, such as,  $AB_1B_3$  and  $AB_1B_4$ .

This approach is further explained the next sub-section and is demonstrated by the construction of a supersonic 3-D wedge followed by a 3-D supersonic caret-shaped geometry. This caret-shaped geometry will then be used to generate supersonic star-shaped geometries of interest.

#### 4.1.1 The 2-D forebody construction (side view)

The review of begins with the construction of the supersonic wedge. Established ideal oblique 2-D shockwave relationships are used to construct the supersonic 2-D forebody. There are two ideal oblique shock relationships which can be used, the Theta-Beta Mach relationship, or the Beta-Theta Mach relationship. In this review, the Theta-Beta Mach [3–5] relationship, described in Section 3.2 above is used in the construction of the supersonic 2-D forebody. For a prescribed Mach number, shock angle, Beta, at a given altitude, a wedge angle, Theta, is extracted. The next step is to set a forebody length. Having all the geometric data the 2-D forebody with the attached shock is constructed as presented in **Figure 6**.

#### 4.1.2 The 2-D inlet construction (side view)

The inlet construction is an extension of the 2-D forebody construction. The oblique shock  $AB$  hits the cowl lip at point  $B$  and is reflected as shown in **Figure 6**.

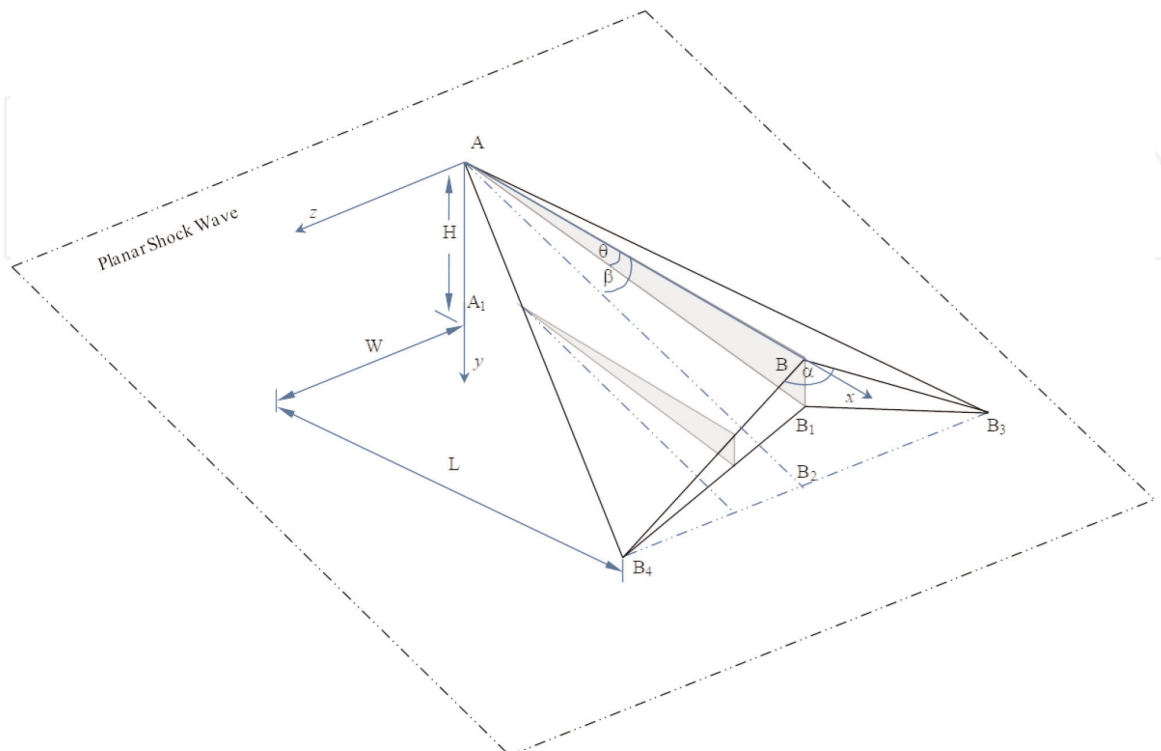


**Figure 5.**  
Nonweiller caret wing waverider configuration.

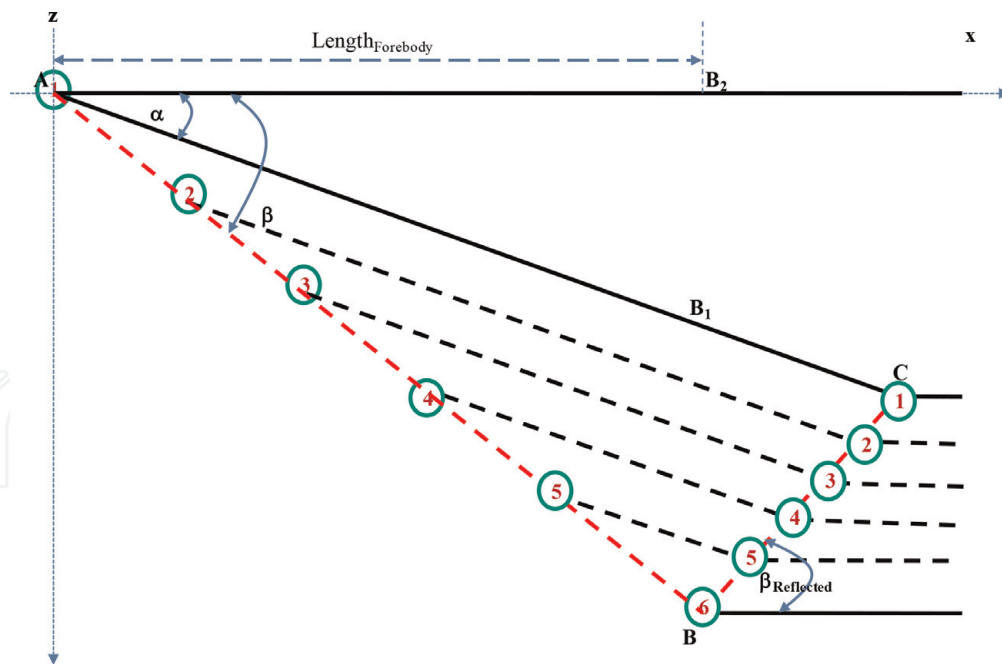


**Figure 6.**  
 Preparation for extracting information for 2-D base view.

Line BC represents the reflected shock from the interaction of the oblique shock and the cowl lip. Ideal oblique shock relationships are used to determine the reflected shock angle, Beta reflected. Note that the line AB<sub>1</sub> which represents the lower surface of the forebody continues to point C where it intersects with line BC. At this point in the design process the 2-D forebody and the inlet are constructed.

#### 4.1.3 Streamline preparation of flow-field

A 2-D base view of the forebody-inlet components are constructed from geometric information obtained from the 2-D side view. The streamline cross-marching method used preserves both the geometric information and the 2-D flow-field information. The oblique shockwave, line AB, is first divided up into *N* number of equal parts, in this case six, as seen in **Figure 6**. Streamlines are then constructed emanating from the oblique shockwave. Each streamline has a starting point on the oblique shockwave, and ends on the reflected shockwave, line BC as presented in **Figure 6**. The longest streamline is represented by line AC and is the lower surface of the forebody-inlet. The shortest streamline is represented by point 6; here the streamline starts and stops at the same point. The streamlines emanating from the oblique shockwave and ending on the reflected shockwave travel parallel with respect to the lower surface of the forebody-inlet as presented in **Figure 6**. All streamlines are now processed by the reflected shockwave, BC, and travel parallel to the surfaces beginning at points C and B as shown in **Figure 6**. The 2-D base view can be extracted from the flow field.

#### 4.1.4 Wedge geometry extraction from flow-field

The base view for the 2-D wedge is now extracted for the 2-D forebody-inlet and the associated 2-D flow-field. A zy-coordinate system is set up and a wedge width is prescribed. Streamlines emanating from the reflected shockwave, BC, are now mapped onto the zy-coordinate system as presented in **Figure 7**. Having completed the construction of the 2-D side view and the 2-D base view, the designer now has

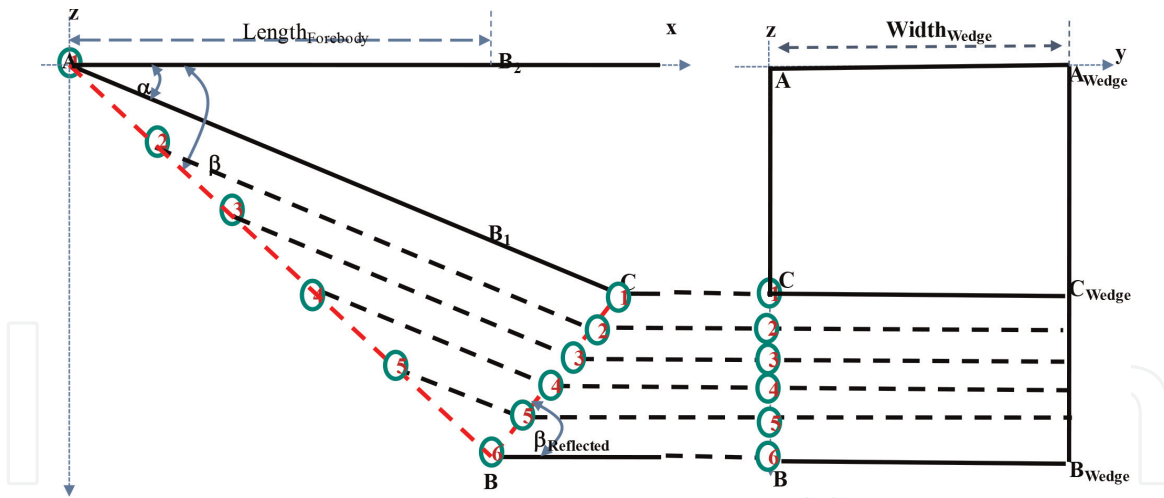


**Figure 7.**  
Generation of 2-D base view for a wedge.

the 3-D coordinates that can be used to generate the 3-D forebody-inlet geometry for a 3-D wedge.

#### 4.2 The caret geometry

The caret geometry forms the basis of the design of the star shaped geometries in this study. A similar process is used to obtain the caret-shaped 2-D base view. Now instead of providing a wedge width, a star angle, Phi, is provided as presented in **Figure 8**. For the four-point-star, Phi is 45 degrees. Reflecting points  $AB_{Point}C$ , about the z-axis will generate the 2-D base view for the caret-shaped waverider geometry. As before, all data required for the 3-D construction of the 3-D caret-shaped forebody-inlet have been extracted from the flow-field. **Figures 9–12** present the 3-D caret-shaped geometry obtained by using the design process described above and programmed using FORTRAN90/95.

#### 4.3 3-D stream tube construction using the waverider approach

The scramjet forebody-inlet-isolator design concept as being proposed suggests a new use for waverider geometries. Here, the focus is not only of the waverider

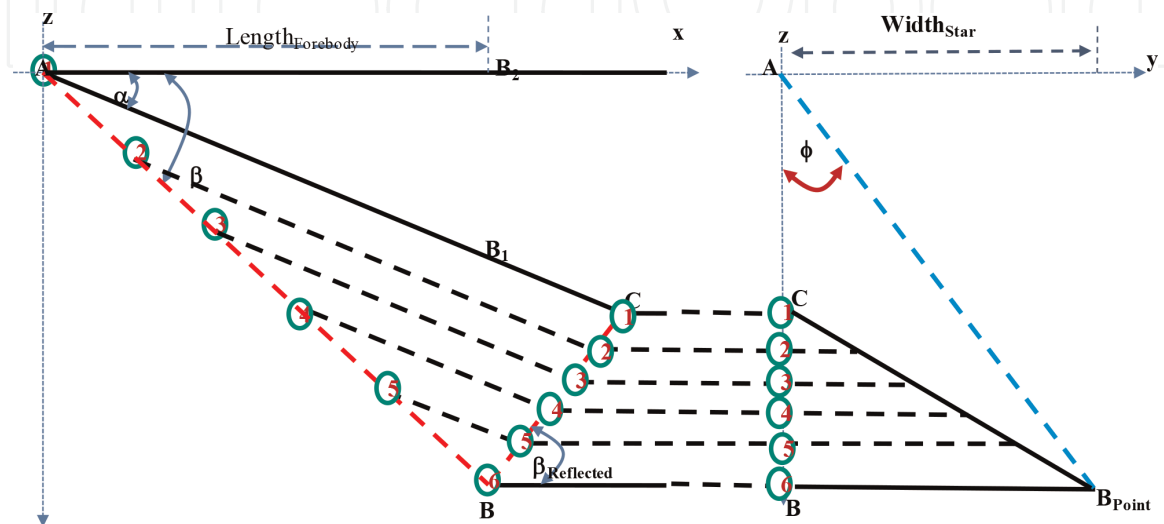


**Figure 8.**  
Generation of 2-D caret-shaped geometry, base view.

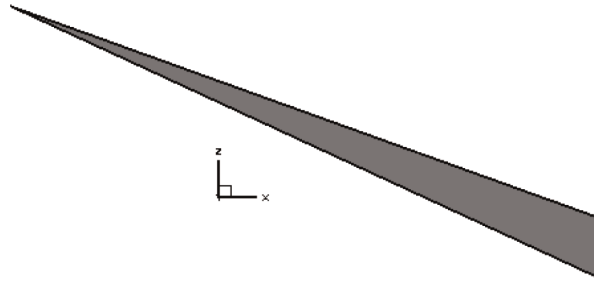


**Figure 9.**  
*Caret 2-D side view.*

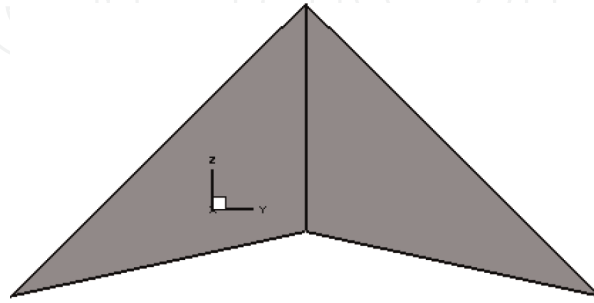


**Figure 10.**  
*Caret 2-D base view.*

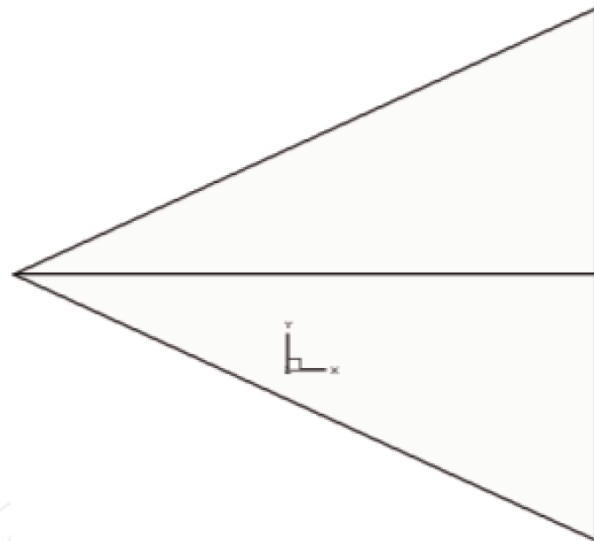


**Figure 11.**  
*Caret 2-D plan view.*

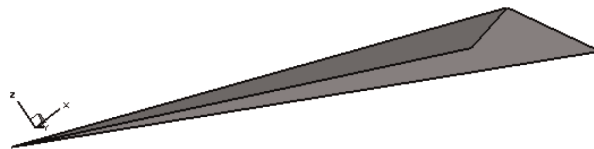


**Figure 12.**  
*Caret 2-D isometric view.*

shape, but also on the external flow-field supporting the waverider configuration. As seen in **Figure 5**, attention is on the external 2-D flow on the waverider lower surfaces, that is,  $AB_1B_3$  and  $AB_1B_4$ , and the flow entering and exiting the planes,  $AB_3B_4$  and  $B_1B_3B_4$ . With this alternative perspective, the innovation lies in the fact that the flow moving across the lower surface of the waverider is treated as the flow

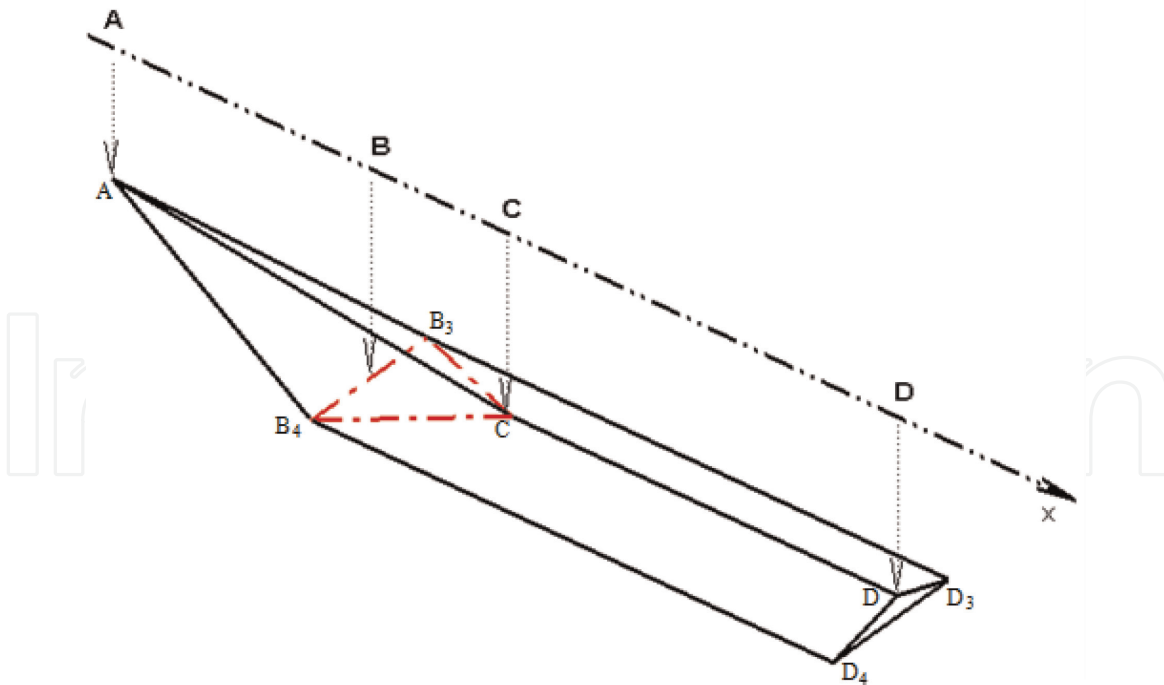


**Figure 13.**  
*Waverider derived stream tube.*

entering a stream tube through surface,  $AB_3B_4$  and leaving through the plane,  $B_1B_3B_4$ . Recall at this point that the flow-field is two dimensional, confined to the  $xy$ -plane and can be treated as a collection of 2-D slices that are parallel to each other. The flow within the stream tube is bounded by the lower inviscid surfaces,  $AB_1B_3$  and  $AB_1B_4$  and an imaginary line surface,  $B_3B_4$ .

A completed stream tube consisting of the forebody-inlet-isolator sections is presented in **Figure 13**. This stream tube is carved/extracted from a supersonic flow-field travelling parallel to the  $x$ -axis, which is compressed by two oblique shock waves; resulting in the flow once again traveling in a direction parallel to the  $x$ -axis. Further examination of **Figure 13** identifies the primary shock wave plane as  $AB_3B_4$ , which supports two compression surfaces,  $ACB_3$  and  $ACB_4$ . At this stage the flow field is no longer parallel to the  $x$ -axis. A reflected shock wave is constructed to form the plane,  $CB_3B_4$ . This specially designed plane,  $CB_3B_4$ , now straightens the flow leaving the shock surface,  $CB_3B_4$ , so that it once again travels parallel to the  $x$ -axis. The reflected flow now forms the stream tube comprising of the following planar surfaces,  $CDD_3B_3$ ,  $CDD_4B_4$ , and  $B_3B_4D_4B_3$ .

#### 4.4 Transforming stream tubes to 'star' shaped geometries

The preceding section saw the design of a single stream tube. These single stream tubes can now be used to create star-shaped geometries of interest, an example of which is presented in **Figure 14**. Presented in **Figure 14** is a four point star geometry, so termed because it is a collection of four stream tubes that is assembled in a manner to create a 'closed form' geometry of interest.

The fundamental concept in moving from a 2-D geometry, **Figure 4**, to the 3-D geometries, **Figures 13–16**, lies mainly on identifying the coordinates along the  $z$ -axis. Determination of the location of points,  $B_3$ ,  $B_4$ ,  $D_3$  and  $D_4$ , is of significant importance. These points are responsible for the development of a closed form geometry/closed tube with the ability of preserving the aerodynamics associated with the inviscid flow-field behavior. Additionally, the ' $y$ ' and ' $z$ ' coordinates of these points rely of the choice of angle  $\alpha$ , an example of which is the angle  $D_3DD_4$  as

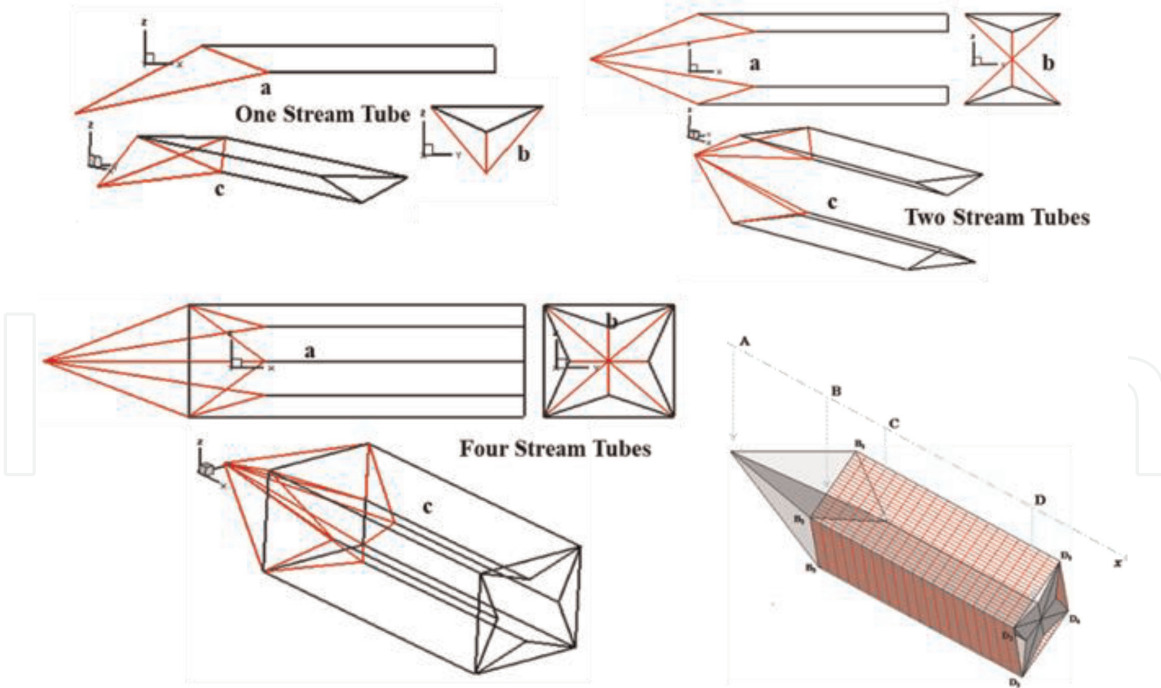


**Figure 14.**  
 A 4-points star-shaped scramjet forebody-inlet-isolator [1].

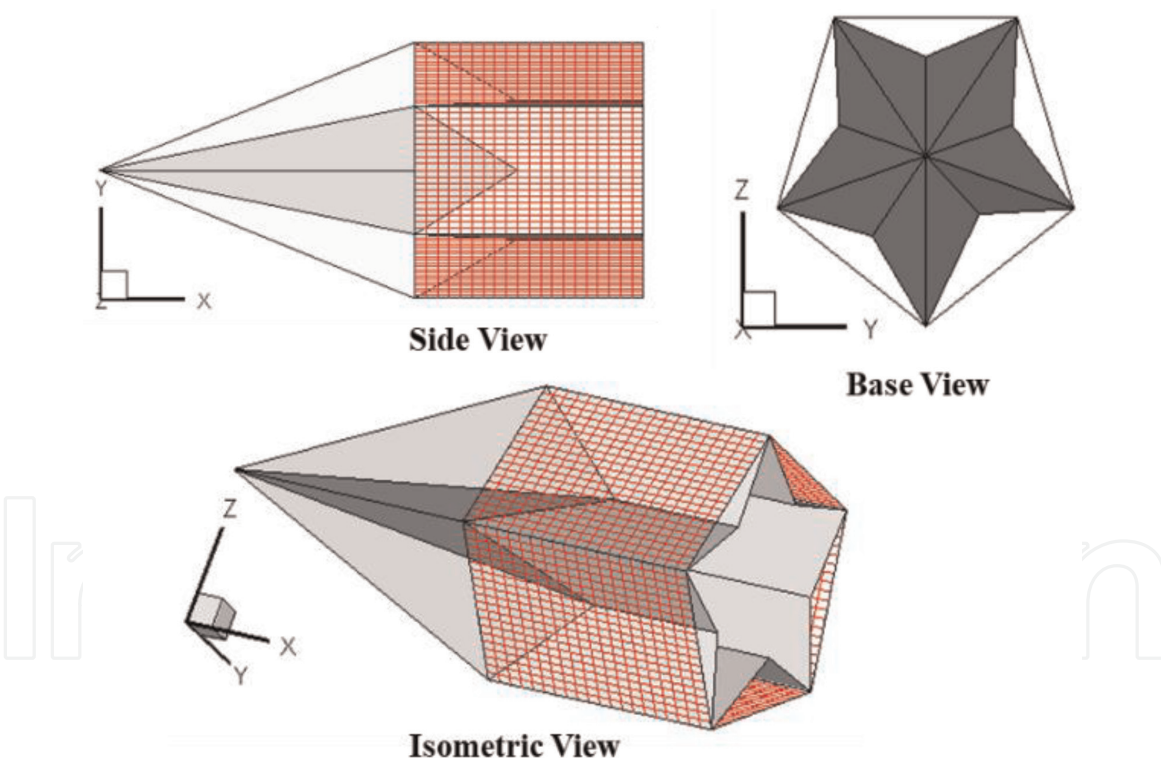


**Figure 15.**  
 Five-points scramjet forebody-inlet-isolator [1].

seen in **Figure 13**. In generating the four point star configuration the angle  $\alpha$  is set to 90 degrees.

## 5. Validation section

This section focuses on the validation of the forebody-inlet-isolator sections associated with the proposed scramjet engine concept. The independent

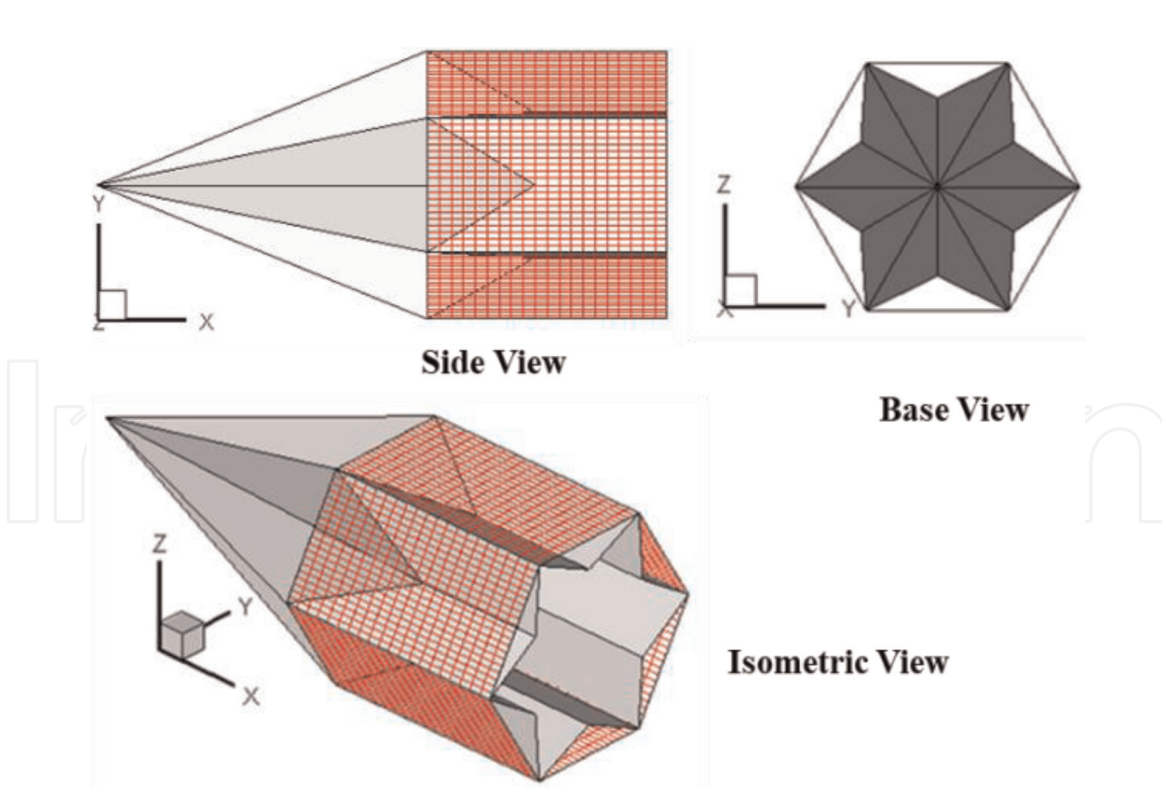


**Figure 16.**  
*Six-points scramjet forebody-inlet-isolator [1].*

Computational Fluid Dynamics (CFD) test studies fall into two categories; 2-D simulations and 3-D simulations.

### 5.1 2-D simulations

Both Euler and viscous studies were conducted on the scramjet forebody, inlet, and isolator sections. 2-D Euler flow studies were conducted using the air vehicles unstructured solver (AVUS) [11]. AVUS is a three-dimensional finite volume unstructured-grid Euler/Navier-Stokes flow solver. 2-D isolator viscous simulations were conducted using an in-house computational scheme, the integral differential scheme (IDS) [12]. The following contour plots (**Figures 17–19** and **24–29**) represent the solution of the AVUS software, whose units are in the SI. Whereas the contour plots shown in **Figure 20** depict the solution of the IDS. The IDS is built on the premise of reducing numerical and modeling errors. As such, the IDS

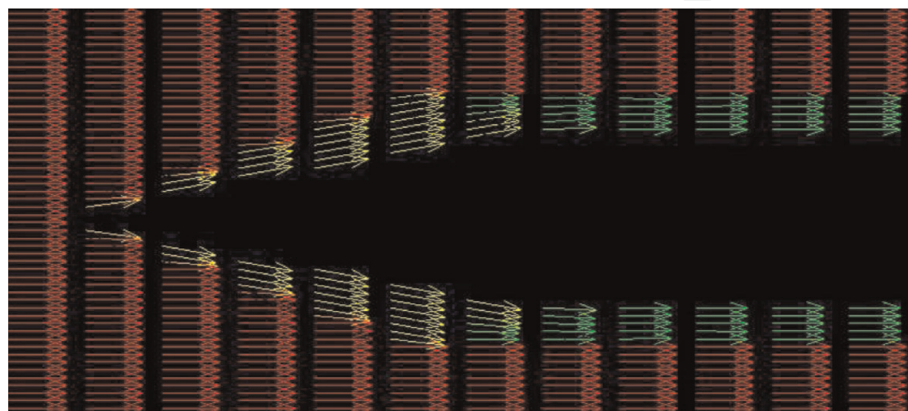


**Figure 17.**  
*AVUS Euler results velocity distribution.*

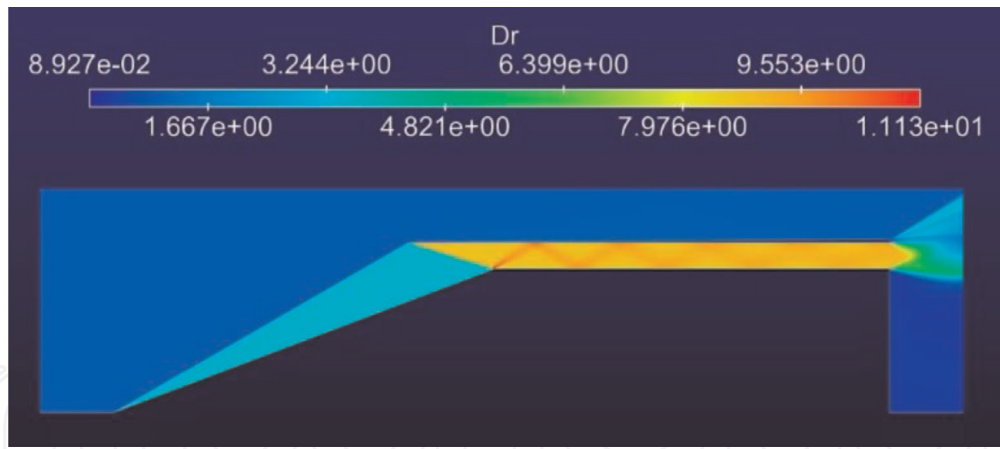


**Figure 18.**  
 AVUS Euler results density contours.

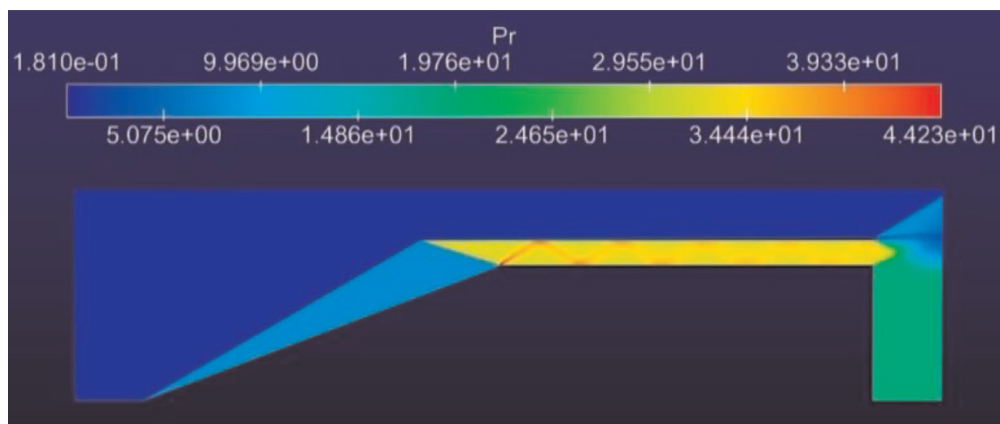
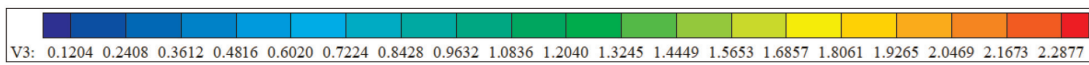
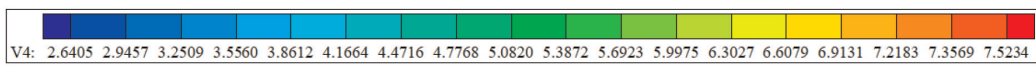


**Figure 19.**  
 AVUS Euler results pressure contours.

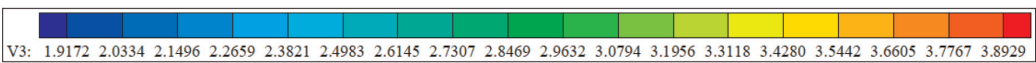
**Mach Number Distribution**



**Pressure Distribution**



**Density Distribution**



**Temperature Distribution**

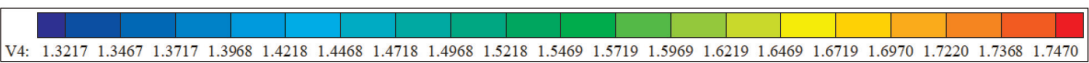


**Figure 20.**  
 Results from isolator 2-D IDS simulation.

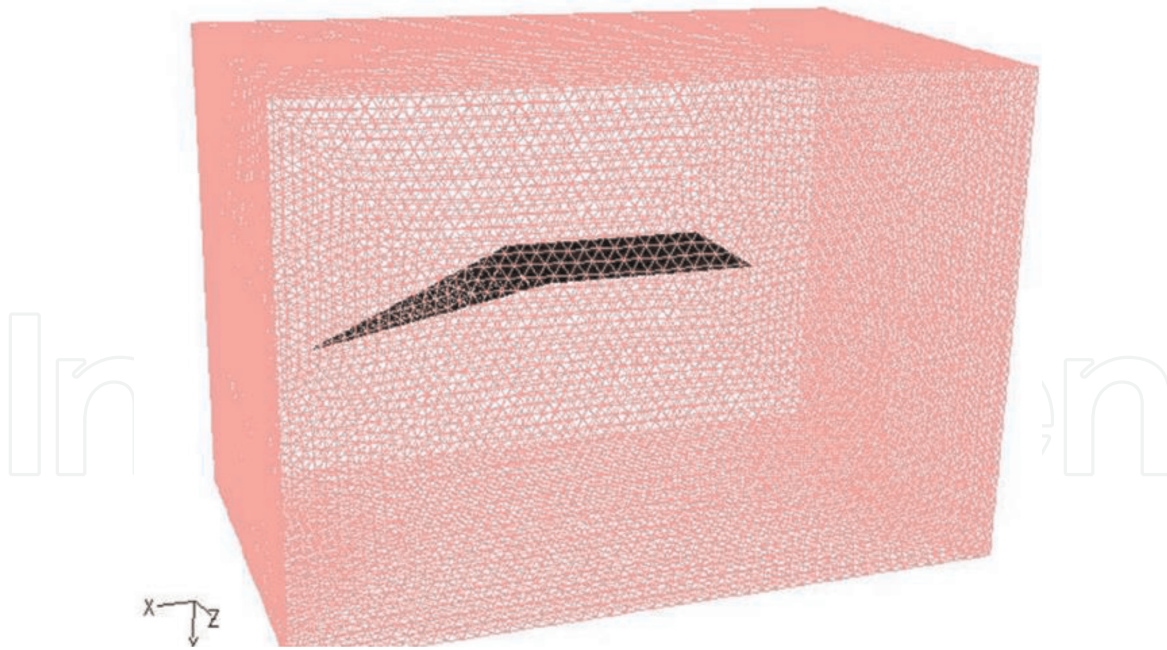


**Figure 21.**  
*3-D stream tube in computational domain.*

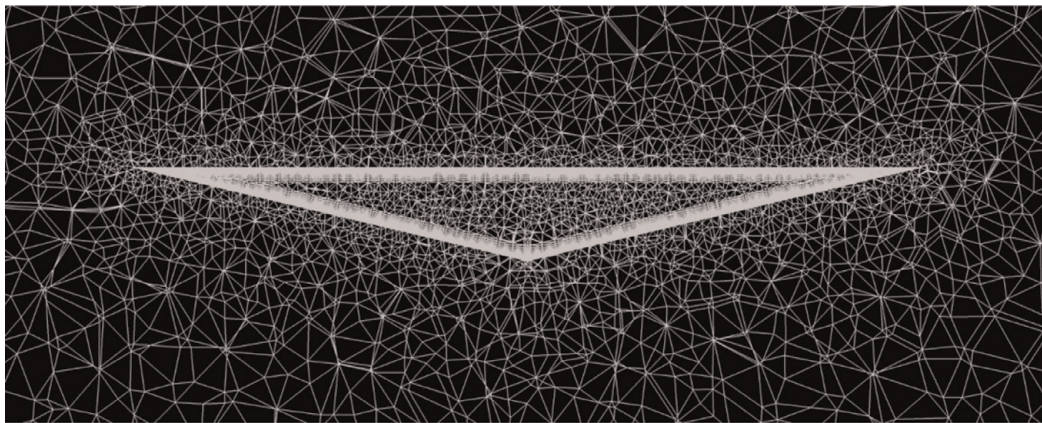


**Figure 22.**  
*3-D stream tube cross-section (isolator exit) with clustering unstructured grids.*

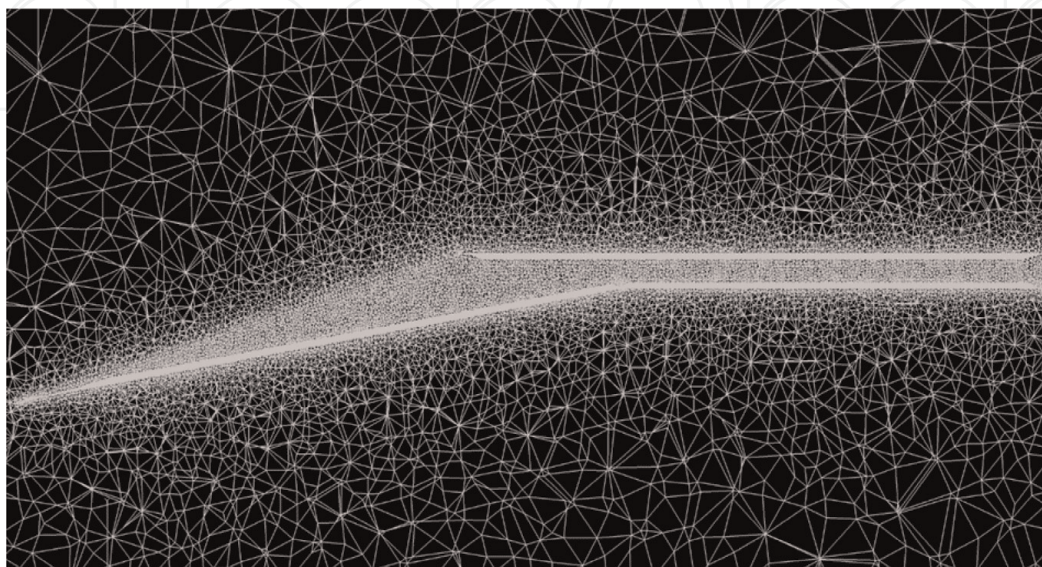


**Figure 23.**  
*3-D stream tube centerline with clustering unstructured grids.*

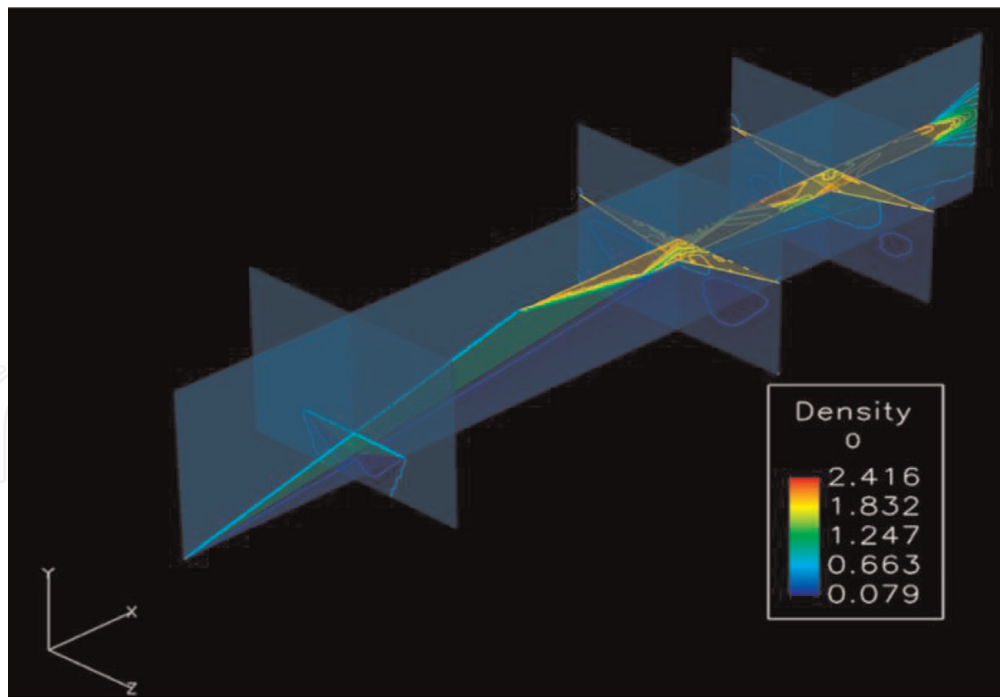


**Figure 24.**  
*Forebody-inlet-isolator validation study with 2-D slices.*

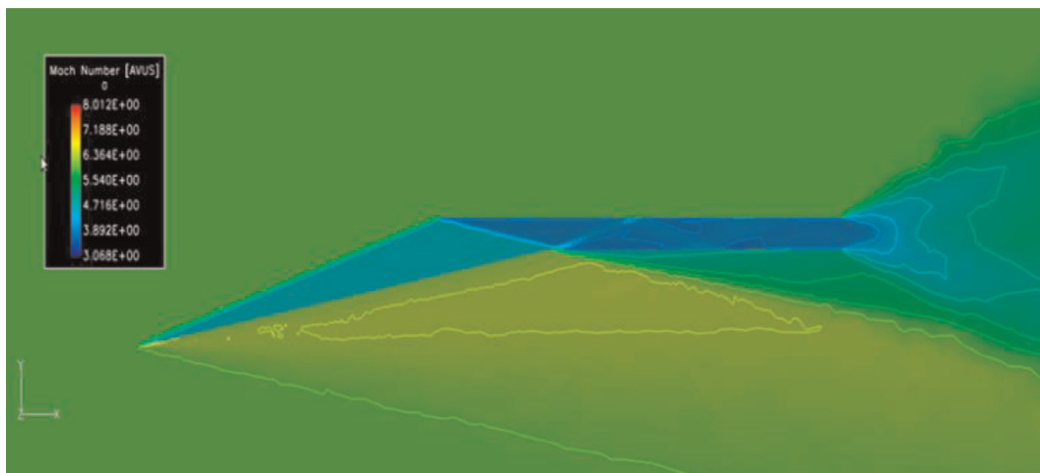


**Figure 25.**  
*Centerline 2-D Mach number contours.*

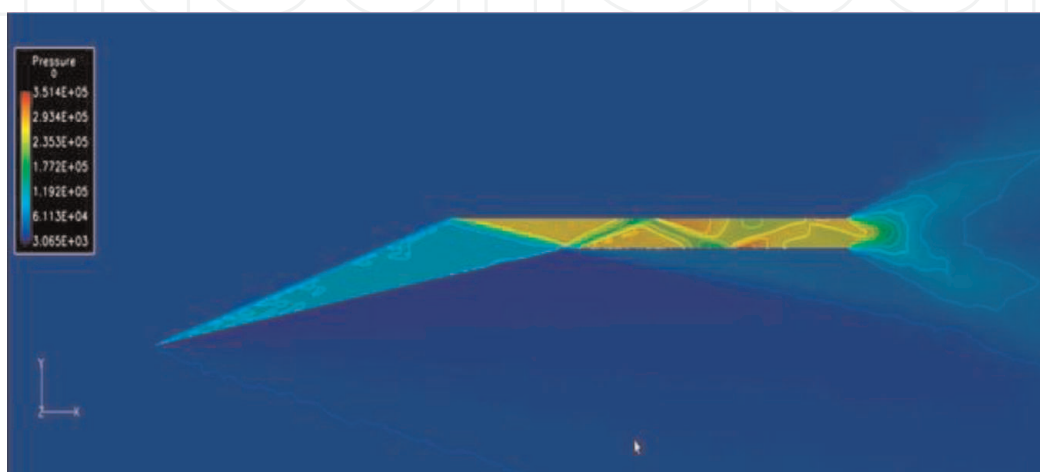


**Figure 26.**  
*Centerline 2-D pressure contours.*

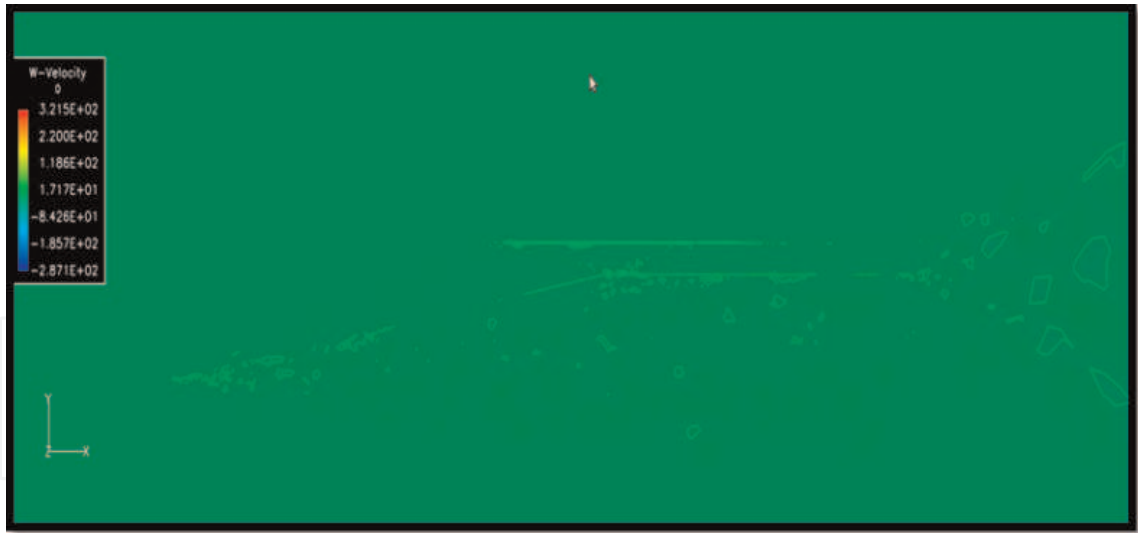


**Figure 27.**  
*Centerline z-component velocity contours.*

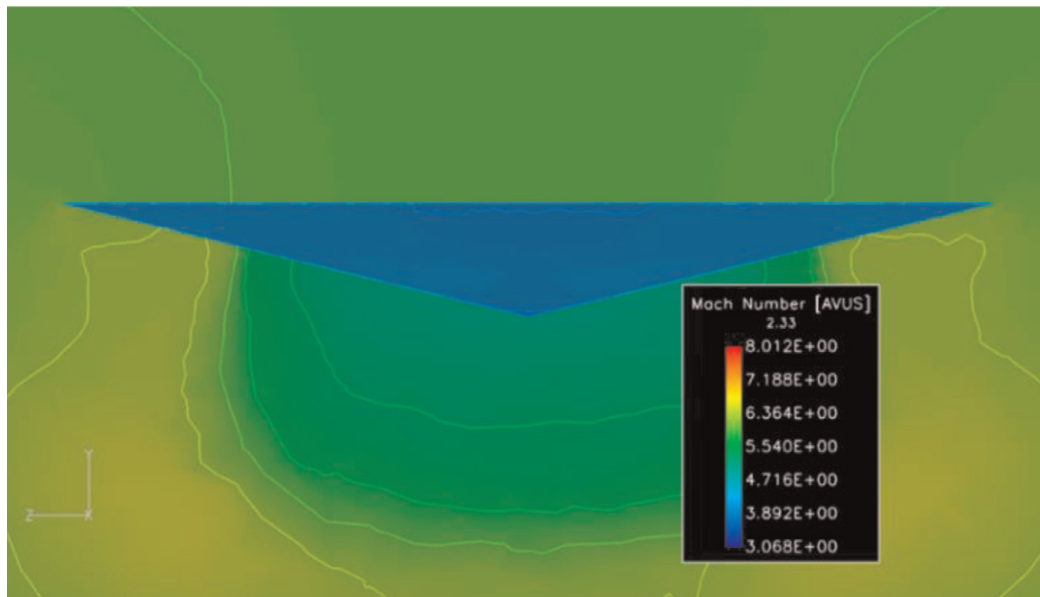


**Figure 28.**  
*Mach contours at the isolator exit.*

implements the dimensionless form of the Navier Stokes equations, and therefore it reduces the round-off error.

### 5.1.1 2-D Euler simulations using AVUS

The four-point star configuration, **Figure 14**, was selected as the test case. The scramjet forebody-inlet-isolator model was exposed to a Mach 5 hypersonic freestream flow-field at a zero angle of attack. **Figures 17–19** presents the 2-D Euler simulation results along the centerline of the four point star configuration. On examining these figures, the following observations are made. **Figure 17** presents velocity distribution data for the geometry, where it is observed that the behavior of the flow imitates the conceptual flow-field presented in **Figure 4**. That is, freestream flow is first processed by the 2-D oblique shock, travels parallel to the wedge surface, is processed again by the reflected shock and travels parallel to the isolator duct walls. **Figures 18 and 19** presents the density and pressure flow-field

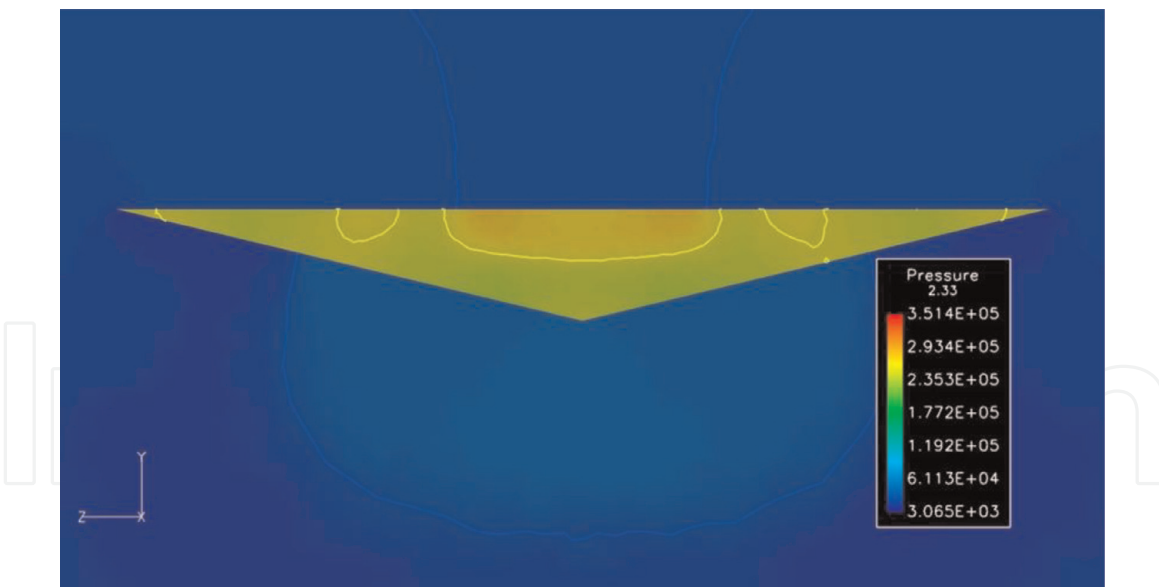


**Figure 29.**  
*Pressure contours at the isolator exit.*

distributions. Once more we observe the organized nature of the 2-D flow, which is supported by the constant property in the respective zones. The development of the shock train within the isolator duct is also captured in these figures.

### 5.1.2 2-D isolator viscous simulations

A 2-D viscous simulation was conducted on the isolator section using the integral differential scheme (IDS), currently under development at North Carolina Agricultural & Technical State University. At the heart of the IDS numerical scheme is the unique combination of both the differential and integral forms of the Navier-Stokes equations (NSE). The differential form of the NSE is used for explicit time marching, whereas integral form of the NSE is used to evaluate the spatial fluxes. The IDS scheme has the ability to capture the complex physics associated with fluid flows. It does this by using a ‘method of consistent averages’ (MCA) procedure which ensures the continuity of the numerical flux quantities. The objective of this initial simulation was to observe the flow behavior. Further details on the physics and computational numerical scheme associated with the IDS can be found in [12]. **Figure 20** presents the flow-field distribution. Flow-field properties presented in **Figure 20** include Mach number distribution, pressure distribution, density distribution, and temperature distribution. Examination of these flow-field properties supports the fact that the flow-field is behaving in a manner as it was designed to.

## 5.2 3-D simulations

3-D computational simulations were also conducted on the scramjet forebody, inlet, and isolator sections. Computational tools used were Fluent and AVUS. In the case of the 3-D Euler computational simulation, a single 3-D stream tube, **Figure 13**, was exposed to a Mach 6 flow-field. The simulation was first conducted using Fluent, where the process is summarized by **Figures 21–23**. Examining **Figures 22** and **23** demonstrates the use of unstructured grids with clustering in key areas for the analysis. The 3-D simulation required 6.7 million elements, 1,165,267 nodes, and 14.75 GB memory. To aid with visualization, 2-D slices, such as those seen in **Figure 24**, were extracted for analysis.

A similar process was implemented with AVUS and 2-D slices of flow-field data are extracted and presented in **Figures 25–29**. On examining these 2-D slices of 3-D data, it is observed that the stream tube is processing the flow in an organized consistent manner that is aligned with its design. Of note are **Figures 27–29**. **Figure 27** examines the z-component of the velocity, and indicated that there is very little cross-flow. Arguable, this is an Euler analysis, however it is worth pointing out that the stream tube 2-D design process holds. This is further supported by **Figures 28 and 29** which presents data on the Mach and pressure distribution at the isolator exit.

## 6. Combustor diffuser nozzle sections

A dual mode scramjet configuration, as presented in **Figure 30**, in addition to having a fore-section consisting of a forebody, inlet, isolator sections; also has an aft-section consisting of a combustor, diffuser and nozzle sections. Whilst the focus of this chapter has been on the design of the fore-section, a brief discussion on the design of the aft-section and its integration is warranted for the sake of completion in the design of the dual mode scramjet.

Design of the aft-section focuses on four fundamental design sections; a transition section, a combustor section, a diffuser section and a nozzle section, **Figures 31 and 32**. The transition section, as implied in the name, is designed to prepare the

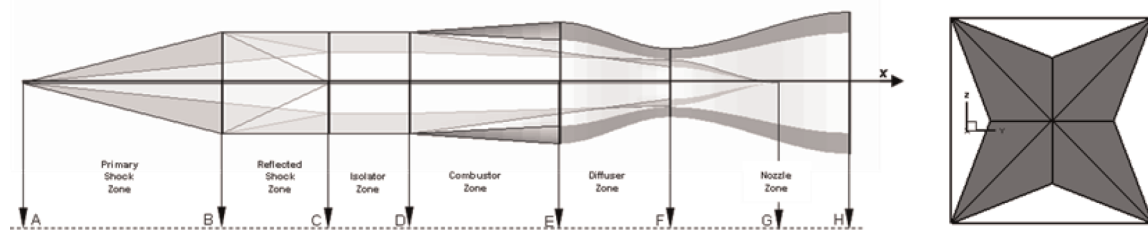


**Figure 30.**  
*A dual mode ramjet-to-scramjet concept [1].*

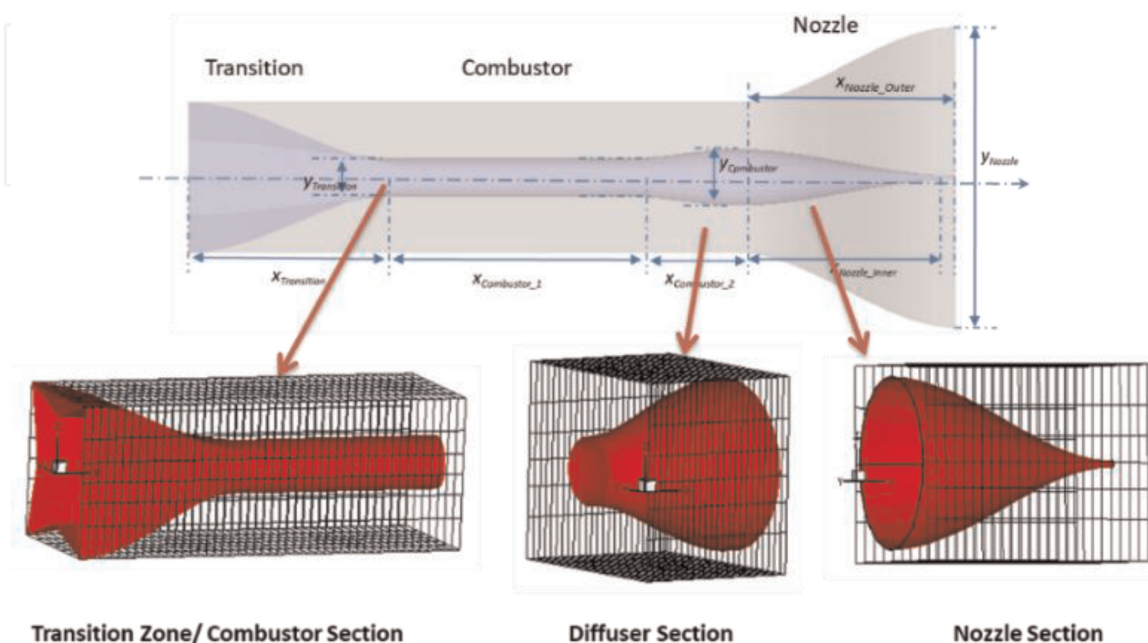


**Figure 31.**  
*2D-3D geometric construction from prescribes isolator cross-section and aerodynamic inputs [1].*

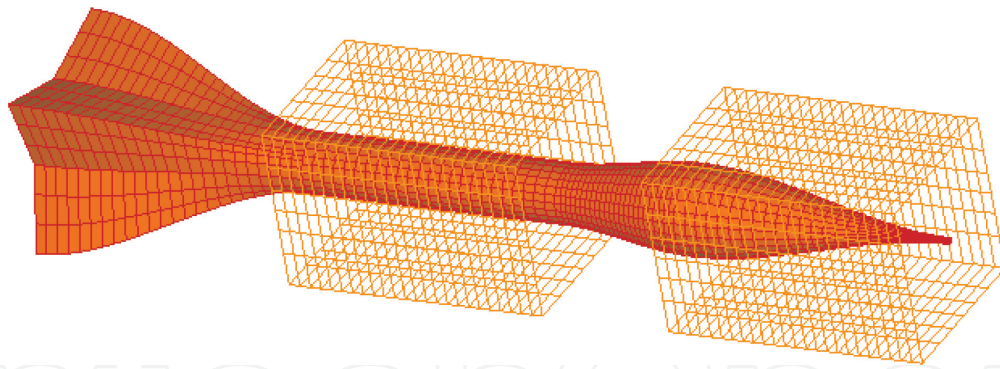


**Figure 32.**  
*Illustration of the transition-combustor-nozzle element.*

flow before it enters the combustor. This section takes the flow leaving the isolator duct and guides it towards combustor. The primary design goal is to ensure that the flow entering the combustor is as organized as possible. The combustion section is where fuel is added, mixed and burned. The diffuser section is used to help control the combustion process as the scramjet operates across its dual mode, that is, switching from ramjet mode to scramjet mode. The nozzle section is used to accelerate the exhaust gases as the flow leaves the dual mode scramjet.

## 7. Scramjet flow-path

A completed scramjet flow-path can now be obtained with the assembly of both the forebody-inlet-isolator and combustor-nozzle sections. Two samples are presented in **Figures 33** and **34**. **Figure 33** presents a scramjet that has a square combustor configuration and **Figure 34**, a circular combustor configuration. Referring back to **Figure 2(c)**, one can observe that a variety of geometries can be

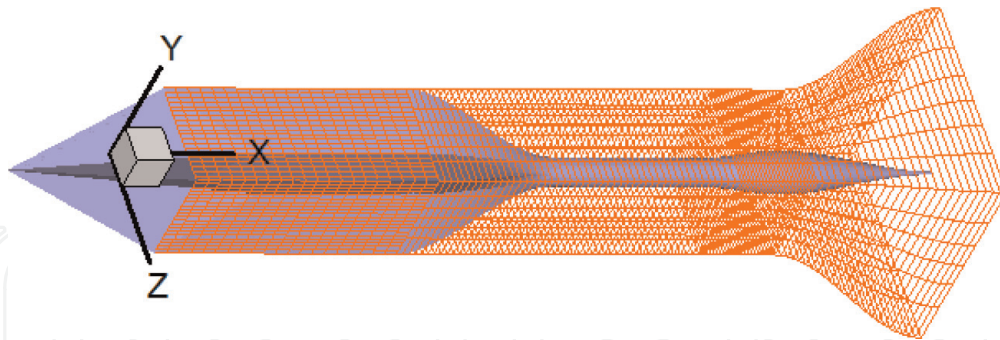


**Figure 33.**  
*4-pts scramjet with square combustor C-sections.*

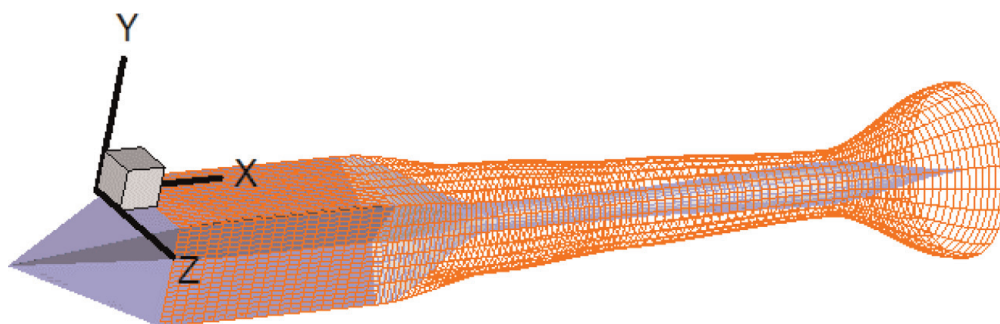


**Figure 34.**  
*4-pts scramjet with circular combustor C-sections.*

generated by manipulating the design points A through H, and the design variables,  $x_3$ – $x_{11}$ , in any combination.

## 8. Conclusion

In this chapter we explored an inverse design approach used in designing scramjet configurations. The forebody, inlet and isolator sections formed the core focus of the chapter. Ideal oblique 2-D shock relations along with Billig's isolator relations were first used to generate a centerline 2-D geometry. Streamline marching techniques coupled with Nonweiler's caret waverider theory were used to geometrically construct 3-D stream tubes. These 3-D stream tubes were later used in the construction of various star-shaped forebody-inlet-isolator sections. Initial 2-D Euler and 2-D viscous studies were performed on the forebody-inlet-isolator sections and the results presented. Initial 3-D Euler studies were also conducted on a single 3-D stream tube. All results presented demonstrated the uniform nature of the flow-field within the stream tube, supporting the inverse design approach. A 3-D viscous analysis of the 3-D stream tube is yet to be undertaken.

## Acknowledgements

Special appreciation is extended to Dr. Isaiah Blankson of NASA Glenn Research Center for his continued guidance. The authors will also like to acknowledge the contributions made by the graduate students who have contributed to this on-going research effort. These include, Thomas Lawrence, Honest F. Mrema, Jovan Brown, Jamil Grant, and Nastassja Dasque.

## Author details

Mookesh Dhanasar<sup>1</sup>, Frederick Ferguson<sup>1</sup> and Julio Mendez<sup>2\*</sup>

<sup>1</sup> North Carolina Agricultural and Technical State University, Greensboro, North Carolina, United States of America

<sup>2</sup> Corredesa LLC, Tyrone, Georgia, United States of America

\*Address all correspondence to: [jcmendez@aggies.ncat.edu](mailto:jcmendez@aggies.ncat.edu)

## IntechOpen

© 2019 The Author(s). Licensee IntechOpen. This chapter is distributed under the terms of the Creative Commons Attribution License (<http://creativecommons.org/licenses/by/3.0>), which permits unrestricted use, distribution, and reproduction in any medium, provided the original work is properly cited. 

## References

- [1] Dhanasar M. Development of A Benchmark for the Design and Analysis of A Tip-To-Tail Ramjet-Scramjet Propulsion System [dissertation]. Greensboro: North Carolina Agricultural and Technical State University; 2009
- [2] Ferguson F, Dhanasar M, Williams R, Blankson I, Kankam D. Supersonic and hypersonic slender air-breathing configurations derived from 2D Flow-fields. In: 46th AIAA Aerospace Sciences Meeting and Exhibit; 7–10 January 2008; Reno, NV. DOI: 10.2514/6.2008-163
- [3] Anderson JD. Fundamentals of Aerodynamics. 3d ed. New York: McGraw-Hill; 2001
- [4] Anderson JD. Hypersonic and High Temperature Gas Dynamics. American Institute of Aeronautics and Astronautics. Virginia, USA: McGraw-Hill; 1989
- [5] Anderson JD. Modern Compressible Flow: With Historical Perspective. 3rd ed. New York, USA: McGraw-Hill; 2004
- [6] Heiser WH, Pratt DT. Hypersonic airbreathing propulsion. AIAA Education Series. Virginia, USA: American Institute of Aeronautics and Astronautics; 1994. ISBN: 1-56347-035-7
- [7] Curran ET, Murthy SNB. Scramjet Propulsion. Vol. 189. Virginia, USA: AIAA; 2000. ISBN: 1-56347-322-4
- [8] Billig FS. Research on supersonic combustion. *Journal of Propulsion and Power*. 1993;9(4):499-514
- [9] Waltrup PJ, Billig FS. Prediction of recompression wall pressure distributions in scramjet engines. *Journal of Spacecraft and Rockets*. 1973; 10(9):620-622
- [10] Nonweiler TRF. Aerodynamic problems of manned space vehicles. *Journal of the Royal Aeronautic Society*. 1959;63:521-528
- [11] Air Force Research Laboratory, CFD Research Branch, Wright-Patterson AFB, OH, Air Vehicles Unstructured Solver (AVUS)
- [12] Ferguson F, Mendez J, Dodoo-Amoo D. Evaluating the hypersonic leading-edge phenomena at high Reynolds and Mach numbers. In: *Recent Trends in Computational Science and Engineering*. Rijeka, Croatia: IntechOpen; 2017